# Average-atom model combined with the hypernetted chain approximation applied to warm dense matter

**4 authors**, including:

Yong Hou
National University of Defense Technology
**23** PUBLICATIONS **148** CITATIONS

SEE PROFILE

Jianmin Yuan
National University of Defense Technology
**233** PUBLICATIONS **1,858** CITATIONS

SEE PROFILE

# Average-atom model combined with the hypernetted chain approximation applied to warm dense matter

Yong Hou,[1,2,*] Richard Bredow,[2] Jianmin Yuan,[1,3] and Ronald Redmer[2]

[1]*Department of Physics, College of Science, National University of Defense Technology, 410073 Changsha, People's Republic of China*
[2]*Institute of Physics, University of Rostock, 18051 Rostock, Germany*
[3]*IFSA Collaborative Innovation Center, Shanghai Jiao Tong University, Shanghai 200240, People's Republic of China*

We have combined the average-atom model with the hypernetted chain approximation (AAHNC) to describe the electronic and ionic structure in the warm dense matter regime. On the basis of the electronic and ionic structures, the x-ray Thomson scattering (XRTS) spectrum is calculated using the random-phase approximation. While the electronic structure is described within the average-atom model, the effects of other ions on the electronic structure are considered using an integral equation method of the theory of liquids, namely the hypernetted chain approximation. The ion-ion pair potential is calculated using the modified Gordon-Kim model based on the electronic density distribution. Finally, the electronic and ionic structures are determined self-consistently. The XRTS spectrum is calculated according to the Chihara formula, where the scattering contributions are divided into three components: elastic, bound-free, and free-free. Comparison of the present AAHNC results with other theoretical models and experimental data shows very good agreement. Thus the AAHNC model can give a reasonable description of the electronic and ionic structure in warm dense matter.

PACS number(s): 52.25.Jm, 52.25.Os, 52.27.Aj, 52.27.Gr

## I. INTRODUCTION

Warm dense matter (WDM) [1] refers to conditions between the physical regimes of condensed matter and weakly coupled plasmas, with temperatures from a few to a few hundred electronvolts (eV) and densities from a few hundredths to about a hundred times solid density. Understanding the physical properties of WDM, such as the equation of state, the radiation opacity, and the transport properties, is crucial for modeling astrophysical objects [2,3] and inertial confinement fusion (ICF) experiments [4]. However, describing WDM faces great challenges since partial ionization, electron degeneracy, bound-state level shift, pressure ionization [5,6], and ion-ion strong coupling must be taken into account in a consistent way. In particular, the accurate description of the coupled electron-ion system is of paramount important for WDM states.

Quantum molecular-dynamics (QMD) [7–11] simulations, which treat the nuclei classically and the electrons quantum mechanically by using finite-temperature density-functional theory (DFT), have proven to yield an appropriate description of the physical properties of WDM. Path integral Monte Carlo or molecular-dynamics simulations [12–17] also give an *ab initio* description of WDM. However, these first-principles methods are computationally expensive, which limits their applicability as a fast analysis tool. Orbital-free molecular dynamics (OFMD) [18–20], where the electronic free energy is a local functional of the electron density, can be used to compute the physical properties at high temperatures. However, at present OFMD is capable of simulating only about $10^3$ atoms. The average-atom (AA) model, which divides the plasma into neutral Wigner-Seitz cells, is also a quite popular method in describing warm and hot dense plasma. In a Wigner-Seitz cell, a nucleus of charge $Z$ and $Z$ electrons are included. The nucleus is fixed in the origin and the electrons are described by

the semiclassical Thomas-Fermi (TF) approximation [21], the quantum-mechanical Schrödinger equation, or the relativistic Dirac equation. Many different versions of the AA model have been implemented [21–29]. Furthermore, the hypernetted chain (HNC) approximation was developed to calculate the structure of classical liquids. It yields reasonable results even for strongly coupled systems [30–34]. This method has also been used to describe the ion structure in the WDM regime, where the interparticle potential is obtained from the finite-temperature Lindhard dielectric response function [35–38].

Spectrally resolved x-ray Thomson scattering (XRTS) experiments [39–45] have shown that important plasma parameters such as temperature, density, and average ionization degree can be determined in WDM. At the same time, different theoretical methods [38,46–51] have been used to interpret the XRTS signal via the dynamic structure factor. The dynamic structure factor is usually calculated according to the Chihara formula [52,53], which divides the scattering into three components: elastic, bound-free, and free-free. The elastic component stems from photons elastically scattered off electrons either localized at the ions or screening the ion charge. The bound-free and free-free components are the contributions of photons inelastically scattered by bound and free electrons, respectively. The free-free scattering contribution can be described using the random-phase approximation (RPA) or the Born-Mermin approximation (BMA), which includes the effects of electron-ion collisions based on Mermin's dielectric function; see Ref. [54].

In the present study, we first investigate the electronic and ionic structure by combining the average-atom model [27,55] with the hypernetted chain approximation (AAHNC) in the WDM regime, and then we calculate the XRTS spectrum based on the results of AAHNC. The structure of bound electrons is obtained by solving the Dirac equation in the central field approximation. Free electrons are computed using the TF approximation, where we consider the ionic structure effects via the HNC approximation. The ionic pair potentials

*yonghou@nudt.edu.cn

are obtained from the electronic density distributions of two isolated ions based on a modified temperature- and density-dependent Gordon-Kim model [56]. The results obtained from this model are in excellent agreement with the known equation of state and ionic structures for Al and Fe [57]. When we calculate the electronic structure, the ionic structure is considered; at the same time, when calculating the ion-ion pair potential, the electronic structure is needed. This problem is solved self-consistently. On the basis of the electronic and ionic structures obtained from AAHNC, the dynamic structure factors are calculated according to the Chihara formula [52,53]. The static ion structure factors are determined in the HNC approximation, and the electronic densities and bound-free transitions are obtained from the modified AA model [27,55], which considers the effects of other ions. We describe the free-free scattering contribution using the RPA, which is sufficient for the conditions considered here.

In the next section, we give a detailed description of the AAHNC method and the equations for the dynamic structure factor. In Sec. III, we apply these methods to calculate the electronic and ionic structures. We give results for the ion-ion structure factor, the average ionization degree, and the XRTS spectra for warm dense Al. Finally, we give a summary.

## II. THEORETICAL METHODS

### A. Average-atom model combined with the hypernetted chain approximation

For an isolated atom or ion, the electron density is calculated by using the modified AA model [27,55], which considers the electron energy level broadening and includes the temperature and density effects on the electronic distributions in a statistical way. Each ion or atom is described in the ion sphere, and in the central-field approximation the bound electrons are described by the Dirac equation:

$$\frac{dP_{n\kappa}(r)}{dr} + \frac{\kappa}{r}P_{n\kappa}(r) = \frac{1}{c}[\epsilon_{n\kappa} + c^2 - V(r)]Q_{n\kappa}(r), \quad (1)$$

$$\frac{dQ_{n\kappa}(r)}{dr} - \frac{\kappa}{r}Q_{n\kappa}(r) = -\frac{1}{c}[\epsilon_{n\kappa} - c^2 - V(r)]P_{n\kappa}(r). \quad (2)$$

$P_{n\kappa}(r)$ and $Q_{n\kappa}(r)$ are, respectively, the large and small components of the wave function of orbital $n\kappa$, $c$ is the speed of light, and $V(r)$ is the self-consistent potential, which has the form [35]

$$V(r) = -\frac{Z}{r} + \int \frac{\rho_b(r')}{|\vec{r} - \vec{r}'|}d^3r' + V_{\mathrm{xc}}[\rho_b(r) + \rho_e^0] - V_{\mathrm{xc}}(\rho_e^0)$$
$$- \frac{\rho_e^0}{\beta}\int C_{\mathrm{ee}}(|\vec{r} - \vec{r}'|)h_{\mathrm{ie}}(r')d^3r'$$
$$- \frac{\rho_i^0}{\beta}\int C_{\mathrm{ie}}(|\vec{r} - \vec{r}'|)h_{\mathrm{ii}}(r')d^3r'. \quad (3)$$

The first four terms constitute the single ionic contribution, namely the electron-nucleus potential, the electrostatic repulsion with the other bound electrons, and the exchange and correlation potential, which are evaluated by using the local density approximation (LDA). The last two terms in Eq. (3) represent interactions with the surrounding free electrons and other ions, respectively. Because $V(r)$ depends on the

electron density and the correlation functions, the solution of Eqs. (1)–(3) has to be done self-consistently if we know the correlation functions. In local thermodynamic equilibrium, the potential at the ion-sphere boundary is chosen as the common reference point in the AA model in order to obtain the same electron density at the boundary for all ions. In this way, we define electrons with energies larger than zero as *free* and with negative energies as *bound*. In our AA model, the boundary conditions are the same as Eqs. (3) and (4) in Ref. [27] when we solve Eqs. (1) and (2), where the bound state orbitals are broadened to energy bands, and the density of bound electrons is computed as

$$\rho_b(r) = \frac{1}{4\pi r^2}\sum_j \int_{\epsilon-3\Delta\epsilon}^{\epsilon+3\Delta\epsilon} b_j(\epsilon)\big[P_j^2(r) + Q_j^2(r)\big]d\epsilon, \quad (4)$$

where $b_j(\epsilon)$ is the density of the occupation number of the state $j$ expressed in terms of the density of states and the Fermi-Dirac distribution,

$$b_j(\epsilon) = \frac{2|\kappa_j|\rho(\epsilon)}{\exp[(\epsilon - \mu)/k_B T] + 1}. \quad (5)$$

The density of states $\rho(\epsilon)$ is taken to be a Gaussian function centered at the corresponding electron orbital energy. It satisfies the requirement that

$$1 = \int_{\epsilon-3\Delta\epsilon}^{\epsilon+3\Delta\epsilon} \rho(\epsilon)d\epsilon, \quad (6)$$

where $\Delta\epsilon$ is the full width at half-maximum of the energy band, and it depends on the two orbital energies obtained with two kinds of boundary conditions [27]. Free electrons are considered much simpler using the TF approximation, and the free electron density is calculated with a Fermi-Dirac distribution in momentum space,

$$\rho_f(r)$$
$$= \frac{1}{\pi^2}\int_{k_0(r)}^{\infty} \frac{k^2 dk}{\exp\{[\sqrt{k^2c^2 + c^4} - c^2 - V(r) - \mu]/k_B T\} + 1}, \quad (7)$$

where $k_0(r) = [2V(r)c^2 + V(r)^2]^{1/2}/c$ and $\mu$ is the chemical potential. The total electron density of the isolated ion or atom is the sum of the bound and free terms: $\rho_{\mathrm{tot}}(r) = \rho_b(r) + \rho_f(r)$. The chemical potential $\mu$ is determined such that electrical neutrality in the ion sphere is guaranteed,

$$\int_0^{r_b} 4\pi r^2 \rho_{\mathrm{tot}}(r)dr = Z, \quad (8)$$

where $Z$ is the nuclear charge and $r_b$ is the ion-sphere radius determined by the plasma density. Thus, the average charge $Z^* = Z - N_b$ can be defined as the nuclear charge $Z$ minus the number $N_b$ of all bound electrons in the ion sphere. In our calculation, the correlation functions extend to the whole space, but we only consider correlation effects inside the ion sphere when calculating the electron structure of the isolated ion.

We define the ion-electron pair correlation function via the excess free-electron density,

$$h_{\mathrm{ie}}(r) = \frac{\rho_f(r)}{\rho_e^0} - 1, \quad (9)$$

where $\rho_e^0$ is the uniform electron density given by $\rho_e^0 = \rho(r_b)$. The ion-ion pair potential is calculated using the modified Gordon-Kim (GK) model [57]. The ion-ion pair potentials are computed via

$$V(R) = V_{\text{Coul}}(R) + V_k(R) + V_e(R) + V_c(R), \quad (10)$$

where $R$ is the distance between the two nuclei, $V_{\text{Coul}}(R)$ is their static Coulomb interaction, $V_k(R)$ is the kinetic energy, and $V_e(R)$ and $V_c(R)$ are the exchange and correlation energies, respectively, which depend on the electron density $\rho(r)$. The static Coulomb potential can be calculated directly from the electron density according to the GK model [56]. The difference between the present model and the original GK model is that the electronic density of the single ion is divided into two parts, namely the uniformly distributed free-electron sea $\rho(r_b)$ and the quasilocalized electrons $\rho_i^{\text{loc}}(r)$, shown in Appendix A; see Ref. [57]. The kinetic energy $E_k(\rho)$, exchange energy $E_e(\rho)$, and correlation energy $E_c(\rho)$ [56,58–60] are computed based only on the electron densities in the spheroidal coordinate system, $\lambda_1 = (r_1 + r_2)/R, \lambda_2 = (r_1 - r_2)/R$.

The ion-ion and free electron-electron correlation functions are calculated using the HNC approximation ($a = e, i$),

$$h_{aa}(r) = \exp[-\beta V_{aa}(r) + h_{aa}(r) - C_{aa}(r)] - 1, \quad (11)$$

and the Ornstein-Zernike relation in Fourier space,

$$h_{aa}(k) = C_{aa}(k)\big[1 + \rho_a^0 h_{aa}(k)\big], \quad (12)$$

where $\rho_a^0$ is the average density for the electrons and ions. The pair potential between free electrons is considered using the Deutsch formula [30],

$$V_{\text{ee}}^{\text{Deutsch}}(r) = \frac{e^2}{4\pi\varepsilon_0 r}\left[1 - \exp\left(-\frac{r}{\lambda_{\text{ee}}}\right)\right]$$
$$+ k_B T \ln 2 \exp\left[-\frac{\ln 2}{\pi}\left(\frac{r}{\lambda_{\text{ee}}}\right)^2\right], \quad (13)$$

with $\lambda_{\text{ee}} = \hbar/\sqrt{m_e k_B T}$. This potential includes quantum effects such as the uncertainty principle and exchange interactions that lead to its temperature dependence.

The flow chart for calculating the electronic and ionic structure self-consistently is explained in Appendix B.

### B. Calculation of the dynamic structure factor

To compare with experimental XRTS spectra, the dynamic structure factor $S(k,\omega)$ has been calculated for WDM. In the AA model, we distinguish between bound and free electrons when calculating the self-consistent electron structure. According to the Chihara formula [38,52], $S(k,\omega)$ can be calculated as the sum of three terms:

$$S(k,\omega) = |f_I(k) + q(k)|^2 S_{\text{ii}}(k,\omega) + Z_f S_{\text{ee}}(k,\omega) + S_{\text{bf}}(k,\omega). \quad (14)$$

The first term is the elastic component determined by the ion-ion structure factor and electrons localized at the ions. Due to their large mass, the dynamic ion structure factor $S_{\text{ii}}(k,\omega)$ is a very narrow feature in frequency, which can be written as $S_{\text{ii}}(k,\omega) = S_{\text{ii}}(k)\delta(\omega)$. The static structure factor $S_{\text{ii}}(k)$ is calculated from the pair distribution function obtained

in the HNC approximation. The form factors, $f_I(k)$ and $q(k)$, can be calculated by the bound-state density and the free-electron screening cloud around the ion, respectively. In the present work, we compute the term from the electron density distribution inside the Wigner-Seitz sphere via Fourier transform,

$$f_I(k) + q(k) = \frac{4\pi}{k}\int_0^{r_b}[\rho_b(r) + \rho_f(r)]r\sin(kr)dr. \quad (15)$$

The second term is the free-electron scattering contribution, which can be expressed using the plasma dielectric function $\varepsilon(k,\omega)$ [50],

$$S_{\text{ee}}(k,\omega) = -\frac{\varepsilon_0\hbar k^2}{\pi e^2 \rho_e^2}\frac{1}{1 - \exp(-\hbar\omega/k_B T)}\text{Im}[\varepsilon^{-1}(k,\omega)], \quad (16)$$

where the free-electron density $\rho_e$ is considered to be a uniform distribution in the Wigner-Seitz sphere. The dielectric function is calculated using the RPA according to [47,51]

$$\text{Re}\,\varepsilon(k,\omega)$$
$$= 1 + \frac{2}{\pi k^3}\int_0^\infty \ln\left|\frac{(k^2 + 2pk + 2\omega)(k^2 + 2pk - 2\omega)}{(k^2 - 2pk + 2\omega)(k^2 - 2pk - 2\omega)}\right|$$
$$\times F(p)p\,dp, \quad (17)$$

$$\text{Im}\,\varepsilon(k,\omega) = \frac{2k_B T}{k^3}\ln\left[\frac{1 + \exp[(\mu - a^2/2)/k_B T]}{1 + \exp[(\mu - b^2/2)/k_B T]}\right], \quad (18)$$

where $a = |2\omega - k^2|/2k$, $b = (2\omega + k^2)/2k$, and $F(p)$ is the free-electron Fermi distribution function. Collisions in the plasmas are neglected in the RPA while the Born-Mermin approximation (BMA) includes collision effects through the ion-electron collision frequency [50].

The third term is the bound-free component, which describes bound electrons ionized by photons in the scattering process. In the AA model, $S_{\text{bf}}(k,\omega)$ is calculated via the matrix elements for transitions between bound and free electrons [47],

$$S_{\text{bf}}(k,\omega) = \sum_m \int \frac{p\,dp}{(2\pi)^3}\left|\int d^3r\,\psi_p^\dagger(\mathbf{r})e^{i\mathbf{k}\cdot\mathbf{r}}\psi_{nlm}(\mathbf{r})\right|^2\Bigg|_{\epsilon=\omega+\epsilon_{nl}}, \quad (19)$$

where $\psi_{nlm}(\mathbf{r})$ and $\psi_p(\mathbf{r})$ are the wave functions of a bound state with quantum numbers $(n,l,m)$ and a continuum state with momentum $\mathbf{p}$, respectively.

### III. RESULTS AND DISCUSSION

#### A. Ion-ion pair distribution function

In partially ionized plasmas, the electronic distribution will be influenced by the ionic structures, and ion-ion interaction potentials are conversely based on the electronic density distribution. In the central-field approximation, the electron density is computed by using the AA model in the self-consistent potential of Eq. (3), where the ionic correlation functions are calculated by the quantum Ornstein-Zernike relation and the HNC closure relation using pair potentials obtained from
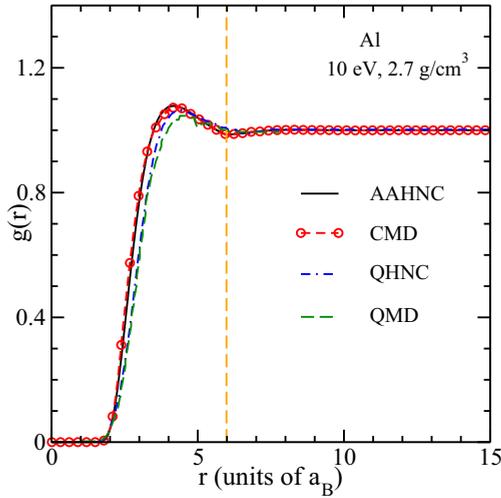
FIG. 1. (Color online) The ion-ion pair distribution functions $g(r)$ for Al at a temperature of 10 eV and a mass density of 2.7 g/cm$^3$. Black solid line: AAHNC result, red dashed line with circles: calculated by classical molecular-dynamics simulations using the ion-ion pair potential from AAHNC, blue dot-dashed line: QHNC result [35], green dashed line: QMD result [48]. The orange dashed line labels the distance of twice the ion-sphere radius.

the modified GK model [57]. The bound-electron density distribution is computed by solving the Dirac equation, and the free-electron density distribution is computed by the TF approximation, i.e., we solve this problem self-consistently; see Appendix B.

First, we present the ion-ion pair distribution functions $g(r)$ for warm dense aluminum at a temperature of 10 eV and a density of 2.7 g/cm$^3$ calculated within the AAHNC model (black solid line) in Fig. 1. QHNC [35] (blue dot-dashed line), quantum molecular dynamics (QMD) [48] (green dashed line), and classic molecular dynamics (CMD) (red dashed line with circles) results are given as well. The QHNC method uses the finite-temperature Lindhard dielectric response function for

the calculation of the ion-ion pair potentials, and it determines the ionic structure through the HNC approximation. The QMD method describes the electronic structure using finite-temperature density-functional theory, and it identifies the ionic structure via classical molecular-dynamics simulations in which the forces onto the ions are determined from the Hellmann-Feynman theorem, i.e., without using pair potentials. The CMD result is obtained based on the converged ion-ion pair potential from the AAHNC result. Figure 1 shows that the AAHNC result agrees well with the CMD curve, i.e., we have successfully combined the AA model with the HNC approximation. However, a slight difference between the AAHNC and the QHNC and QMD results occurs at the first peak that is due to the different approximations for the ion-ion pair potentials.

### B. Average ionization degree

In Fig. 2, we show the average ionization degree of aluminum ions as a function of the density for temperatures of 100 and 10 eV. The black line with circles represents the AAHNC results, and the red line with squares is the result of the AA model without considering the effects of other ions. Both methods include the energy level broadening [27,55].

For 100 eV (left panel) we can see that the average charge decreases with increasing density. Most electrons of an Al atom are ionized at a temperature of 100 eV and low densities. With increasing density, the average frequency of collision between free electrons and ions increases and, as a result, recombination occurs. The two peaks in the lines are signatures of pressure ionization of the $3s$ and $3p$ orbitals that occurs at medium densities. The AAHNC results, considering the effects of other ions, are smaller than those of the AA model in the whole density regime, and pressure ionization is shifted to higher densities. This means that in the AAHNC approximation, electron recombination is stronger so that a greater fraction of free electrons is relocalized in bound states.

Similar results are shown for 10 eV in the right panel of Fig. 2. Before pressure ionization of $2p$ electrons occurs,
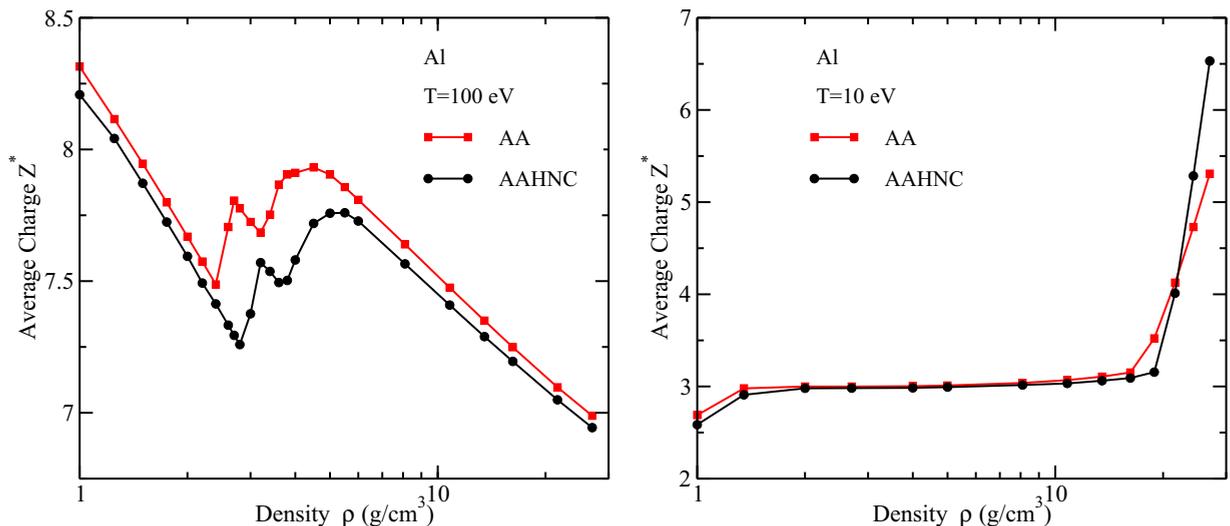


FIG. 2. (Color online) Density dependence of the average ionization degree of Al at a temperature of 100 eV (left panel) and 10 eV (right panel). Black line with circles: AAHNC result, red line with squares: result of the AA model with broadening of the energy levels.

the AAHNC results are also slightly smaller than those of the AA model. However, the AAHNC results become larger after pressure ionization of $2p$ electrons has occurred at about 20 g/cm$^3$ due to the fact that the average ionic distance decreases with increasing density, and ion-ion collisions favor electron ionization. Thus, ionic contributions yield a sharper $2p$ pressure ionization. We conclude that ion correlations affect ionization and recombination in the partially ionized plasma: at low densities, the recombination of free electrons is enhanced, while at high densities electron ionization is enhanced.

### C. X-ray Thomas scattering spectrum

In this section, we discuss the dynamic structure factor $S(k,\omega)$ based on the AAHNC results according to Eq. (14). The free-electron scattering contribution $S_{ee}(k,\omega)$ is expressed in terms of the dielectric function $\varepsilon(k,\omega)$ and calculated in the RPA. The average ionization degree is determined within the AAHNC model. Bound-free transitions are calculated via the matrix elements using the AAHNC results. In Fig. 3, we display the elastic ion feature as a function of $k$ at a temperature of 10 eV and a density of 8.1 g/cm$^3$. To describe different results in the same figure, the static structure factors were multiplied by 20 and the form factors by 5. All black lines with circles in Fig. 3 represent the results of the AAHNC method, red lines with triangles those of QMD [61], and blue lines with squares those of HNC [38]. The static structure factors $S_{ii}(k)$ are shown as dot-dashed lines, total form factors $|f_I(k) + q(k)|$ as dashed lines, and the ion features $|f_I(k) + q(k)|^2 S_{ii}(k)$ as solid lines with the respective color code.

The static structure factors $S_{ii}(k)$ agree well despite a different behavior at low $k$, where the AAHNC method overestimates the isothermal compressibility $S_{ii}$ ($k = 0$). Nevertheless, this difference would not affect the XRTS spectra at
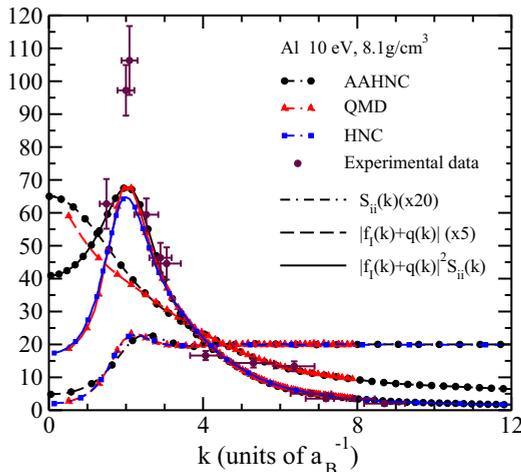
FIG. 3. (Color online) Elastic XRTS contribution for Al as a function of $k$ at a temperature of 10 eV and a density of 8.1 g/cm$^3$: AAHHC (black lines with circles), QMD (red lines with triangles) [61], and HNC (blue lines with squares) [38] results are compared with experimental results (points with error bars) [39]. The static structure factors $S_{ii}(k)$ are shown as dot-dashed lines, total form factors $|f_I(k) + q(k)|$ as dashed lines, and the ion features $|f_I(k) + q(k)|^2 S_{ii}(k)$ as solid lines with the respective color code.

both angles 69° and 111°. $q(k)$ and $f_I(k)$ are the form factors of the screening cloud around the ion and of bound electrons in the ion, respectively. $|f_I(k) + q(k)|$ is calculated from the Fourier transform of the electron density in the Wigner-Seitz sphere according to Eq. (15). The red dashed line with triangles is computed via the Hartree-Fock (HF) approximation [62], which has been used to obtain the elastic ion feature in Ref. [61]. The HF approximation refers to isolated atoms so that plasma effects are not included, which appears to be a small difference from the AAHNC result at low $k$ values.

In Fig. 3, we also display the elastic ion features $|f_I(k) + q(k)|^2 S_{ii}(k)$ calculated by using the AAHNC method (black solid line with circles), QMD (red solid line with triangles) [61], and HNC (blue solid line with squares) [38], respectively, and we compare with experimental results (points with error bars) [39]. Our AAHNC results are in good agreement with the experimental results except for the two highest points. At low $k$, our results are larger than those of the QMD [61] and HNC method [38]; this difference stems from the static ion-ion structure factor and the form factor. However, our result is very similar to that of the QMD at the peak position.

The dynamic structure factors $S(k,\omega)$ at a temperature of 10 eV and a density of 8.1 g/cm$^3$ are calculated from the sum of the three terms according to the Chihara formula, Eq. (14) [52,53], at the scattering angles 69° ($k = 5.44a_B^{-1}$) and 111° ($k = 7.94a_B^{-1}$). The elastic ion feature is calculated as in Fig. 3 for these angles. We determine the bound-free contribution using the bound and free electronic wave functions as obtained from the converged AAHNC results according to Eq. (19) [47].

It has been shown that the difference between the RPA and the BMA is very small for the angles considered here [38], so that we use the RPA to describe the free-free scattering process in the present study. In Fig. 4 (left panel), we show the dynamic structure factor at the scattering angle 69°. The black solid, blue dot-dashed, and red dashed lines denote the present AAHNC results, experimental results [39], and the results of Souza *et al.* [38], respectively. The orange solid and green dashed lines (low) represent bound-free (bf) contributions of our AAHNC method and that of Souza *et al.* [38], respectively; they agree well. We conclude that the present AAHNC results for the XRTS spectra of warm dense Al are in good agreement with experimental and theoretical results.

The right panel in Fig. 4 shows the results for the other angle 111°. The two theoretical results (AAHNC, Souza *et al.*) are again in good agreement. However, a big difference between the experimental and theoretical results occurs. Souza *et al.* [38] have discussed this difference based on the Chihara formula, Eq. (14) [52,53], and they found that the behavior of the free-free contribution and of the elastic-ion feature is not capable of explaining this discrepancy. Our AAHNC method uses the modified GK model [57] to compute the ion-ion pair potentials and the Deutsch potential to calculate the electron-electron correlation function. Therefore, we apply different descriptions for the electronic and ionic structures. However, we obtain similar results compared with the study of Souza *et al.* [38]. Comparing with the experimental results [39], the spectra have been broadened using Gaussian profiles (325 eV full width at half-maximum). A larger width of
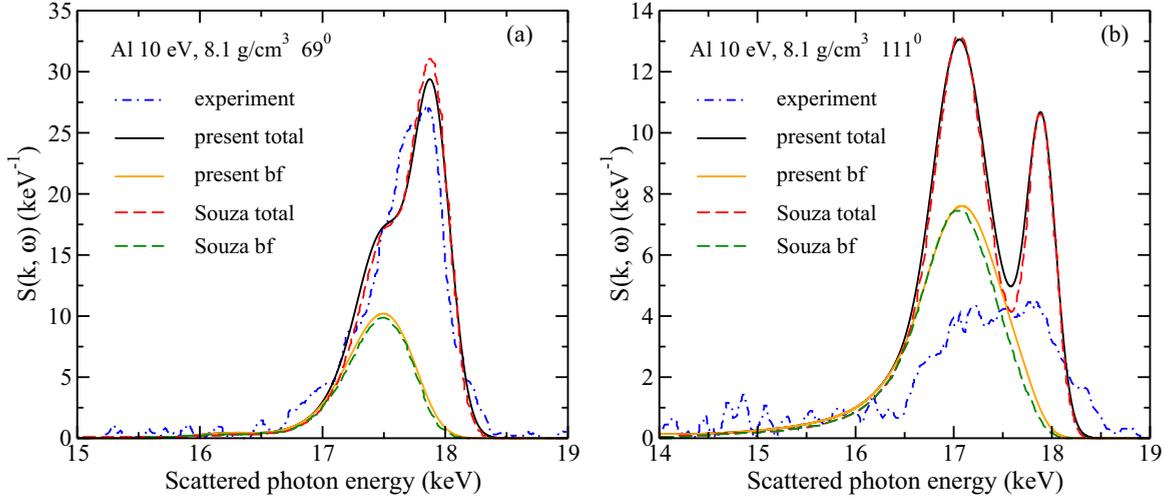
FIG. 4. (Color online) Calculated XRTS spectra for warm dense Al at a temperature of 10 eV and a density of 8.1 g/cm$^3$ compared with experimental results (blue dot-dashed line) [39] at scattering angles 69° (left panel) and 111° (right panel). The black and orange solid lines denote the total spectrum (high) and bound-free (bf) (low) contributions, respectively, calculated from the AAHNC method; the free-free contribution is calculated in the RPA. The red and green dashed lines are, respectively, the total spectrum (high) and the bound-free (low) contributions from Souza *et al.* [38].

the instrumental function may need to be considered when calculating the dynamic structure factor at this larger angle of 111°. This issue has to be addressed in future studies.

### IV. SUMMARY

We have computed the electronic and ionic structures of warm dense aluminum by using the AAHNC model. When calculating the electronic structures within the average-atom model, the ion-ion and ion-electron correlation functions were considered in a self-consistent manner. The consideration of correlation effects of the ions (AAHNC versus the AA model) enhances the recombination of free electrons at high temperatures and, subsequently, the average ionization degree decreases; see Fig. 2. However, at lower temperatures, the opposite behavior arises at high densities because the correlation effects of the ions enhance ionization due to collisions. On the basis of the electronic and ionic structures determined within the AAHNC method, x-ray Thomson scattering spectra were computed using the random-phase approximation for the free-free contribution in the Chihara formula (14). Comparison shows that the AAHNC results are in good agreement with other theoretical approaches [38] and experiments [39]. We conclude that the AAHNC model is a reliable tool for the determination of the electronic and ionic structure in hot and warm dense matter.

### ACKNOWLEDGMENTS

### APPENDIX A: THE MODEL OF THE ION-ION PAIR POTENTIAL

We divide the electron density into two parts: the uniformly distributed free-electron sea $\rho(r_b)$ in the whole space with a density equal to that of the electrons at the ion-sphere boundary $r_b$, and the quasilocalized electrons $\rho_i^{loc}(r)$ representing the dramatic spatial variation of the electronic distribution around the nucleus. The latter quantity is the total density minus the uniformly distributed free-electron density; it is assumed to be unchanged when two ions come closer. The distributions of quasilocalized electrons, labeled by the red dashed line in Fig. 5, will overlap and the total density of the interacting ions is the sum of the two separate ions in the overlap region. To keep the electron density of the uniformly distributed free-electron sea unchanged when the electrons of two ions overlap, the boundary changes in such a way that the truncated spherical volume, labeled by the black solid line in
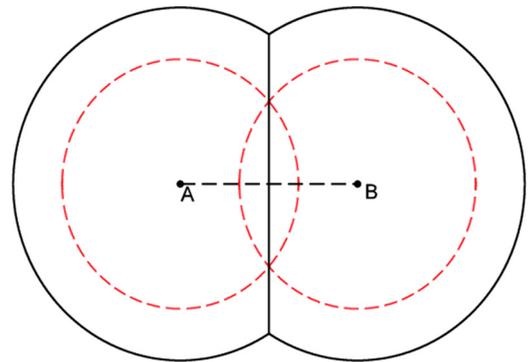


FIG. 5. (Color online) Electron density distribution when two nuclei approach each other; see [57].

Fig. 5, equals the sum of the two separated ions; this ensures electrical neutrality in the whole interaction region. Thus, the total density is $\rho = \rho_A^{\text{loc}} + \rho_B^{\text{loc}} + \rho(r_b)$, where $A$ and $B$ represent the different ions, respectively.

## APPENDIX B: FLOW CHART OF THE CALCULATION

When calculating the electronic and ionic structures, we start with an initial correlation function and calculate the initial electronic potential as shown in Fig. 6. On the basis of this electronic potential, the Dirac equation is solved and the chemical potential is determined according to the electrical neutrality condition in the ion sphere. We recalculate the electronic potential using the old correlation functions repeatedly until a self-consistent electron structure is obtained. Afterward, the ion-ion pair potential is calculated based on this electron structure according to the modified Gordon-Kim method. The new correlation function is obtained within the HNC approximation and compared with the old ones. If the results for the ion structure are not converged, we enter the loop for computing the electron structure again using this new correlation function until converged results for the electron as
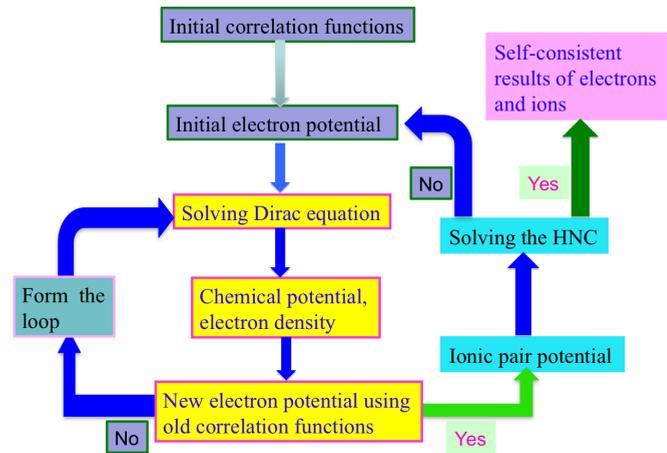


FIG. 6. (Color online) Flow chart for the self-consistent calculation of the electronic and ionic structure in the AAHNC method.

well as the ion structure are obtained. The flow chart of this self-consistent treatment is shown in Fig. 6.

[1] R. W. Lee, H. A. Baldis, R. C. Cauble, O. L. Landen, J. S. Wark, A. Ng, S. J. Rose, C. Lewis, D. Riley, J.-C. Gauthier, and P. Audebert, Laser Part. Beams **20**, 527 (2002).

[2] M. D. Knudson, M. P. Desjarlais, R. W. Lemke, T. R. Mattsson, M. French, N. Nettelmann, and R. Redmer, Phys. Rev. Lett. **108**, 091102 (2012).

[3] D. C. Swift, J. H. Eggert, D. G. Hicks, S. Hamel, K. Caspersen, E. Schwegler, G. W. Collins, N. Nettelmann, and G. J. Ackland, Astrophys. J. **744**, 59 (2012).

[4] B. Remington, R. P. Drake, and D. Ryutov, Rev. Mod. Phys. **78**, 755 (2006).

[5] S. M. Vinko *et al.*, Nature (London) **482**, 59 (2012).

[6] T. R. Preston, S. M. Vinko, O. Ciricosta, H.-K. Chung, R. W. Lee, and J. S. Wark, High Energy Density Phys. **9**, 258 (2013).

[7] M. P. Desjarlais, Phys. Rev. B **68**, 064204 (2003).

[8] F. R. Krajewski and M. Parrinello, Phys. Rev. B **73**, 041105(R) (2006).

[9] T. D. Kuhne, M. Krack, F. R. Mohamed, and M. Parrinello, Phys. Rev. Lett. **98**, 066401 (2007).

[10] S. Mazevet, F. Lambert, F. Bottin, G. Zérah, and J. Clérouin, Phys. Rev. E **75**, 056404 (2007).

[11] J. Dai, Y. Hou, and J. Yuan, Phys. Rev. Lett. **104**, 245001 (2010); Astrophys. J. **721**, 1158 (2010).

[12] W. R. Magro, D. M. Ceperley, C. Pierleoni, and B. Bernu, Phys. Rev. Lett. **76**, 1240 (1996).

[13] B. Militzer and D. M. Ceperley, Phys. Rev. Lett. **85**, 1890 (2000).

[14] A. V. Filinov, M. Bonitz, and Yu. E. Lozovik, Phys. Rev. Lett. **86**, 3851 (2001).

[15] M. A. Morales, J. M. McMahon, C. Pierleoni, and D. M. Ceperley, Phys. Rev. Lett. **110**, 065702 (2013).

[16] D. Kang, J. Dai, H. Sun, Y. Hou, and J. Yuan, Sci. Rep. **3**, 3272 (2013).

[17] D. Kang, H. Sun, J. Dai, W. Chen, Z. Zhao, Y. Hou, J. Zeng, and J. Yuan, Sci. Rep. **4**, 5484 (2014).

[18] F. Lambert, J. Clérouin, and G. Zérah, Phys. Rev. E **73**, 016403 (2006); F. Lambert, J. Clérouin, J.-F. Danel, L. Kazandjian, and G. Zérah, *ibid.* **77**, 026402 (2008).

[19] F. Lambert and V. Recoules, Phys. Rev. E **86**, 026405 (2012).

[20] L. Burakovsky, C. Ticknor, J. D. Kress, L. A. Collins, and F. Lambert, Phys. Rev. E **87**, 023104 (2013).

[21] R. P. Feynman, N. Metropolis, and E. Teller, Phys. Rev. **75**, 1561 (1949).

[22] B. F. Rozsnyai, Phys. Rev. A **5**, 1137 (1972); J. Quant. Spectrosc. Radiat. Transfer **27**, 211 (1982); B. F. Rozsnyai and M. Lamoureux, *ibid.* **43**, 381 (1990).

[23] D. A. Liberman, Phys. Rev. B **20**, 4981 (1979); J. Quant. Spectrosc. Radiat. Transfer **27**, 335 (1982).

[24] T. Blenski and K. Ishikawa, Phys. Rev. E **51**, 4869 (1995).

[25] G. Faussurier, C. Blancard, and A. Decoster, Phys. Rev. E **56**, 3474 (1997); **56**, 3488 (1997).

[26] J. Yuan, Phys. Rev. E **66**, 047401 (2002).

[27] Y. Hou, F. Jin, and J. Yuan, Phys. Plasmas **13**, 093301 (2006).

[28] W. R. Johnson, C. Guet, and G. F. Bertsch, J. Quant. Spectrosc. Radiat. Transfer **99**, 327 (2006).

[29] B. Wilson, V. Sonnad, P. Sterne, and W. Isaacs, J. Quant. Spectrosc. Radiat. Transfer **99**, 658 (2006).

[30] R. Bredow, Th. Bornath, W.-D. Kraeft, and R. Redmer, Contrib. Plasma Phys. **53**, 276 (2013).

[31] K. Wünsch, P. Hilse, M. Schlanges, and D. O. Gericke, Phys. Rev. E **77**, 056404 (2008).

[32] V. Schwarz, Th. Bornath, W.-D. Kraeft, S. H. Glenzer, A. Höll, and R. Redmer, Contrib. Plasma Phys. **47**, 324 (2007).

[33] V. Bezkrovniy, M. Schlanges, D. Kremp, and W.-D. Kraeft, Phys. Rev. E **69**, 061204 (2004).

[34] M. Baus and J. Hansen, Phys. Rep. **59**, 1 (1980).

[35] D. Saumon, C. E. Starrett, J. D. Kress, and J. Clérouin, High Energy Density Phys. **8**, 150 (2012).

[36] C. E. Starrett and D. Saumon, Phys. Rev. E **87**, 013104 (2013).

[37] C. E. Starrett and D. Saumon, High Energy Density Phys. **10**, 35 (2014).

[38] A. N. Souza, D. J. Perkins, C. E. Starrett, D. Saumon, and S. B. Hansen, Phys. Rev. E **89**, 023108 (2014).

[39] T. Ma, T. Döppner, R. W. Falcone, L. Fletcher, C. Fortmann, D. O. Gericke, O. L. Landen, H. J. Lee, A. Pak, J. Vorberger, K. Wünsch, and S. H. Glenzer, Phys. Rev. Lett. **110**, 065001 (2013).

[40] S. P. Regan, K. Falk, G. Gregori, P. B. Radha, S. X. Hu, T. R. Boehly, B. J. B. Crowley, S. H. Glenzer, O. L. Landen, D. O. Gericke, T. Döppner, D. D. Meyerhofer, C. D. Murphy, T. C. Sangster, and J. Vorberger, Phys. Rev. Lett. **109**, 265003 (2012).

[41] C. Fortmann, H. J. Lee, T. Döppner, R. W. Falcone, A. L. Kritcher, O. L. Landen, and S. H. Glenzer, Phys. Rev. Lett. **108**, 175006 (2012).

[42] H. J. Lee, P. Neumayer, J. Castor, T. Döppner, R. W. Falcone, C. Fortmann, B. A. Hammel, A. L. Kritcher, O. L. Landen, R. W. Lee, D. D. Meyerhofer, D. H. Munro, R. Redmer, S. P. Regan, S. Weber, and S. H. Glenzer, Phys. Rev. Lett. **102**, 115001 (2009).

[43] E. G. Saiz, G. Gregori, D. O. Gericke, J. Vorberger, B. Barbrel, R. J. Clarke, R. R. Freeman, S. H. Glenzer, F. Y. Khattak, M. Koenig, O. L. Landen, D. Neely, P. Neumayer, M. M. Notley, A. Pelka, D. Price, M. Roth, M. Schollmeier, C. Spindloe, R. L. Weber, L. van Woerkom, K. Wünsch, and D. Riley, Nat. Phys. **4**, 940 (2008).

[44] A. L. Kritcher, P. Neumayer, J. Castor, T. Döppner, R. W. Falcone, O. L. Landen, H. J. Lee, R. W. Lee, E. C. Morse, A. Ng, S. Pollaine, D. Price, and S. H. Glenzer, Science **322**, 69 (2008).

[45] S. H. Glenzer, G. Gregori, R. W. Lee, F. J. Rogers, S. W. Pollaine, and O. L. Landen, Phys. Rev. Lett. **90**, 175002 (2003).

[46] W. R. Johnson and J. Nilsen, Phys. Rev. E **89**, 023107 (2014).

[47] W. R. Johnson, J. Nilsen, and K. T. Cheng, Phys. Rev. E **86**, 036410 (2012).

[48] K.-U. Plagemann, P. Sperling, R. Thiele, M. P. Desjarlais, C. Fortmann, T. Döppner, H. J. Lee, S. H. Glenzer, and R. Redmer, New J. Phys. **14**, 055020 (2012).

[49] K. Wünsch, J. Vorberger, G. Gregori, and D. O. Gericke, Europhys. Lett. **94**, 25001 (2011).

[50] S. H. Glenzer and R. Redmer, Rev. Mod. Phys. **81**, 1625 (2009).

[51] G. Gregori, S. H. Glenzer, W. Rozmus, R. W. Lee, and O. L. Landen, Phys. Rev. E **67**, 026412 (2003).

[52] J. Chihara, J. Phys. Condens. Matter **12**, 231 (2000).

[53] J. Chihara, J. Phys. F **17**, 295 (1987).

[54] A. Höll *et al.*, High Energy Density Phys. **3**, 120 (2007).

[55] Y. Hou, F. Jin, and J. Yuan, J. Phys. Condens. Matter **19**, 425204 (2007).

[56] R. G. Gordon and Y. S. Kim, J. Chem. Phys. **56**, 3122 (1972); Y. S. Kim and R. G. Gordon, Phys. Rev. B **9**, 3548 (1974).

[57] Y. Hou and J. Yuan, Phys. Rev. E **79**, 016402 (2009).

[58] J. C. Slater, *Quantum Theory of Atomic Structure* Vol. II (McGraw-Hill, New York, 1960).

[59] W. J. Carr, R. A. Coldwell-Horsfall, and A. E. Fein, Phys. Rev. **124**, 747 (1961); W. J. Carr and A. A. Maradudin, *ibid.* **133**, A371 (1964).

[60] Jianmin Yuan, Yijun Zhao, and Zhijie Zhang, Acta Mech. Sin. **21**, 479 (1989) (in Chinese).

[61] H. R. Rüter and R. Redmer, Phys. Rev. Lett. **112**, 145007 (2014).

[62] J. H. Hubbel, W. J. Veigele, E. A. Briggs, R. T. Brown, D. T. Cromer, and R. J. Howerton, J. Phys. Chem. Ref. Data **4**, 471 (1975).